# We are IntechOpen, the world's leading publisher of Open Access books
# Built by scientists, for scientists

## 6,900
Open access books available

## 185,000
International authors and editors

## 200M
Downloads

## 154
Countries delivered to

Our authors are among the

## TOP 1%
most cited scientists

## 12.2%
Contributors from top 500 universities

CLARIVATE ANALYTICS
BOOK CITATION INDEX
INDEXED

**WEB OF SCIENCE**™

Selection of our books indexed in the Book Citation Index
in Web of Science™ Core Collection (BKCI)

# Interested in publishing with us?
# Contact book.department@intechopen.com

# Effects of the Microstructure Induced by Sintering on the Dielectric Properties of Alumina

Zarbout Kamel[1], Moya Gérard[2],
Si Ahmed Abderrahmane[2], Damamme Gilles[3] and Kallel Ali[1]
*[1]Sfax University, LaMaCoP, BP 1171, Sfax 3000,*
*[2]Aix-Marseille University, Im2np, UMR-CNRS 6242, Marseille,*
*[3]Commissariat à l'Energie Atomique, DAM Ile-de-France, Bruyère-le-Châtel*
*[1]Tunisie*
*[2,3]France*

## 1. Introduction

The dielectric properties of undoped corundum, α-alumina, of different kinds (single crystal or polycrystalline obtained by solid state sintering) have been the subject of numerous studies concerning, in particular, the breakdown strength and the charging behavior (Haddour et al., 2009; Liebault et al., 2001; Si Ahmed et al., 2005; Suharyanto et al., 2006; Thome et al., 2004; Touzin et al., 2010; Zarbout et al., 2008, 2010). The common feature pointed out by most of these investigations is the conspicuous role played by the microstructure and the impurities. It is also established that the microstructure induced by the sintering process (grain size and porosity) goes concomitantly along with impurities segregation at grain boundaries and/or the development of defects in the lattice (Chiang et al., 1996; Gavrilov et al., 1999; Lagerlöf & Grimes, 1998; Moya et al., 2003). To some extent, for a given composition, these evolutions can be governed by the sintering conditions, for instance the firing cycle in the case of solid state sintering (Chiang et al., 1996).

The breakdown strength is a key parameter for the reliability of dielectrics and in particular of microelectronic insulator components. This parameter is intimately linked to the charging properties as breakdown originates from the enhancement of the density of trapped charges, which stems from the competition between charge trapping and conduction (Blaise & Le Gressus, 1991; Le Gressus et al., 1991; Liebault et al., 2001; Haddour et al., 2009). The charges can be either generated by irradiation or injected through interfaces via an applied voltage. Charge trapping can occur around intrinsic point defects, defects induced by the dissolution of impurities, defects associated with grain boundaries interfaces and dislocations (Kolk & Heasell, 1980). We must also keep in mind that trapping in insulators gives rise to polarization and lattice deformation allowing energy accumulation within the material (Blaise & Le Gressus, 1991; Le Gressus et al., 1991; Stoneham, 1997). As a result, if some critical density of trapped charges (or some critical electric field) is reached, external stresses (thermal, electrical or mechanical) can trigger a collective relaxation process corresponding

to a release of stored energy. If the amount of this energy is sufficient, breakdown could set in causing irreversible damages of the material (Blaise & Le Gressus, 1991; Moya & Blaise, 1998; Stoneham, 1997).

It appears that an improvement of the breakdown strength would require that conduction, which tends to decrease density of trapped charges, be favored to some extent without, however, substantially altering the insulating properties. Conduction will also be referred as the ability of the material to spread charges. Therefore, the control of the competition between charge accumulation (trapping) and spreading (conduction), via the fabrication processes, is a key technological concern. The foregoing arguments motivate the need to develop methods for the characterization of charge conduction (conversely charge trapping) and underscore furthermore the importance of controlling the microstructural development during sintering of ceramic insulators. The purpose of this chapter is to provide the physical background for a more comprehensive understanding of the effects of the microstructure (and the various defects) induced by the sintering conditions on charge conduction in alumina. This understanding, which could be generalized to other ceramics, appears as prerequisite for the fabrication of insulators of improved dielectric breakdown strength.

## 2. Defects in α-alumina

The α-alumina, exhibits the hexagonal corundum structure. In this structure, $Al^{3+}$ cations occupy only two-thirds of the available sites and an interstitial unoccupied site arises between alternate pairs of $Al^{3+}$. Charge trapping in alumina may take place around defects that can be intrinsic in nature or stemming from the dissolution of impurities (i.e., the foreign cations and their charge compensating defects). In sintered materials, one has also to take into account the effect of grain boundaries, segregation of impurities and defects at interfaces. These defects are characterized by energy levels within the wide band gap (of about 9 eV in alumina).
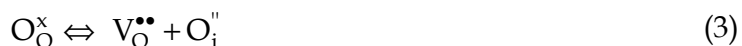
### 2.1 Point defects

### 2.1.1 Intrinsic point defects (Schottky and Frenkel defects)

The Schottky defects consist of pairs of negatively charged cationic vacancies $V_{Al}'''$ and positively charged anionic vacancies $V_O^{\bullet\bullet}$. The vacancies must be formed in the stoichiometric ratio (two aluminium for three oxygen) in order to preserve the electrical neutrality of the crystal. Using the Kröger-Vink notation, the formation of Schottky defects obey to the reaction:

$$2\, Al_{Al}^x + 3\, O_O^x \Leftrightarrow 2\, V_{Al}''' + 3\, V_O^{\bullet\bullet} + Al_2O_3 \tag{1}$$

The Frenkel defects are formed when the $Al^{3+}$ cation (Eq. 2) or the $O^{2-}$ anion (Eq. 3) is displaced from its normal site onto an interstitial site giving a vacancy and an interstitial pair:

$$Al_{Al}^x \Leftrightarrow V_{Al}''' + Al_i^{\bullet\bullet\bullet} \tag{2}$$

$$O_O^x \Leftrightarrow V_O^{\bullet\bullet} + O_i^{''} \tag{3}$$

Simulation results show that the formation energies of intrinsic point defects in α-alumina are relatively high (Atkinson et al., 2003). They are estimated respectively for Schottky defects, cation Frenkel and anion Frenkel at 5.15, 5.54 and 7.22 eV.

### 2.1.2 Extrinsic point defects

Extrinsic point defects are entailed by the dissolution of foreign elements. The solubility of an impurity depends mainly on its cation size (generally, small size elements exhibit high solubility). The charge compensating defects accompanying the dissolution of aliovalent impurities (i.e, defects that are required for ensuring the electrical neutrality) are determined not only by their valence (charge) but also by their position (interstitial or substitutional) in the host lattice.

In the case of a cation (M) greater in valence than the host cation (Al³⁺), the dissolution mode in substitutional position is most likely the cationic vacancy compensation mechanism (Atkinson et al., 2003). Accordingly, for tetravalent cations, in $MO_2$ (such as $SiO_2$ or $TiO_2$), the dissolution reaction is:

$$3\,MO_2 + 4\,Al_{Al}^x \Leftrightarrow 3\,M_{Al}^{\bullet} + V_{Al}^{'''} + 2\,Al_2O_3 \tag{4}$$
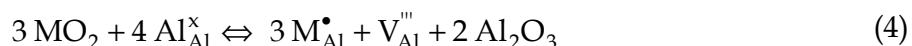
This compensation by a cationic vacancy is somewhat corroborated by experiments involving solution of Ti⁴⁺ in α-Al₂O₃ (Mohapatra & Kröger, 1977; Rasmussen & Kingery, 1970).

For divalent cations, in $MO$ (such as $MgO$ or $CaO$), the anionic vacancy compensation of substitutional $M_{Al}^{'}$, is suggested (Atkinson et al., 2003):

$$2\,MO + 2\,Al_{Al}^x + O_O^x \Leftrightarrow 2\,M_{Al}^{'} + V_O^{\bullet\bullet} + Al_2O_3 \tag{5}$$

The interstitial dissolution of monovalent elements, in $M_2O$ (such as $Na_2O$ or $Ag_2O$), can be governed by a host cationic vacancy compensation mechanism. However, a self-compensating dissolution mode, involving both interstitial and substitutional positions of M, is also expected (Gontier-Moya et al., 2001).

In the case of isovalent elements, in $M_2O_3$ (such as $Cr_2O_3$ or $Y_2O_3$), the dissolution will not create charged defects in the lattice but can induce a stress field due to the misfit arising from the difference in cation radii.

As previously pointed out, the formation energies of intrinsic defects are very high in α-alumina. Consequently, a few ppm of impurities will make the concentrations of extrinsic defects higher than those of the intrinsic ones, even at temperatures near the melting point (Kröger, 1984; Lagerlöf & Grimes, 1998).

### 2.1.3 Point defects association

Isolated point defects can be associated, at appropriate temperature, to form neutral or charged defect clusters. This association leads to a substantial reduction in the solution

energy due to strong coulombic interaction and lattice relaxation. A typical example of defect clustering is the association of defects induced by the dissolution of tetravalent cations (Eq. 4):

$$3\,M_{Al}^{\bullet} + V_{Al}^{'''} \Leftrightarrow (3\,M_{Al}^{\bullet} : V_{Al}^{'''})^{x} \tag{6}$$

Mass action calculations (Lagerlöf & Grimes, 1998) have shown that the relative concentrations of extrinsic defects (point defects and defect associations) depend on the equilibrium temperature under which they are created. In sintered alumina, they can be determined by the sintering temperature and time, i.e. isothermal part of the firing schedule.

### 2.1.4 Association of point defects with charges

Anionic vacancies $V_O^{\bullet\bullet}$ (or cationic vacancies $V_{Al}^{'''}$) can be associated with electrons (or holes) to form F centers (or V centers). In fact, upon trapping one electron (or two electrons), $V_O^{\bullet\bullet}$ becomes a F$^+$ center (or a F center). Anionic vacancies can also be associated with a substitutional divalent cation $M_{Al}^{'}$ to form F$_{cation}$ center (such as F$_{Mg}$ or F$_{Ca}$). The F, F$^+$ and F$_{cation}$ act as a donor centers. The energy levels of F and F$^+$ are respectively estimated around 3 and 3.8 eV below the edge of the conduction band (Kröger, 1984).

### 2.2 Extended defects: Grain boundaries

Grain boundaries are the interfaces between like crystals, at which atomic planes are always disrupted to some extent. The atomic order of the lattice is preserved up to within approximately a unit cell of the dividing plane. Thus, the disordered region of a grain boundary is typically only 0.5 − 1 nm wide, although it does vary somewhat with the type of boundary and the crystal lattice periodicity. Grain boundaries provide segregation sites for impurities and defects.

## 3. Sintering of α-alumina

### 3.1 Sintering of α-alumina and induced microstructure

The polycrystalline alumina samples (of 0.2 cm thickness and 1.6 cm diameter) were processed, at Ecole Nationale Supérieure des Mines "ENSM" of Saint Etienne (France), by sintering from two types of powders of different purities (Table 1). The first referred below as "pure", elaborated by the Exal process and provided by CRICERAM Co., contains about 150 ppm of different impurities (with 90 ppm of silicon). The second referred as "impure", elaborated by the Bayer process and provided by REYNOLDS Co., has an impurity content near 4000 ppm (with 1497 ppm of silicon). In Table 1, the compositions of single crystals, which will be considered as reference material, are also given (cf. next section).

Before sintering, the powders were prepared according to conventional procedures involving successively aqueous dispersion, adding of organic binders, spray drying, uniaxial die forming and cold isostatic pressing. Sintering near theoretical density was performed in air with a firing schedule (Fig. 1), which comprises:

- a binder burnout stage where samples were heated slowly (1 K/min) up to 773 K in three steps during 5 hours,
- a heat-up stage, at 2 K/min, from 773 K to the required sintering temperature $T_s$,
- an isothermal heat treatment at $T_s$ with a dwelling time $t_s$,
- a cooling stage at rate of about 10 K/min.

|  | SiO$_2$ | CaO | MgO | Na$_2$O | Fe$_2$O$_3$ | K$_2$O | Cr$_2$O$_3$ | TiO$_2$ |
|---|---|---|---|---|---|---|---|---|
| **Alumina powders "pure" (Criceram)** | 90 | 5 | < 5 | 40 | 12 | --- | --- | --- |
| **Alumina powders "impure" (Reynolds)** | 1497 | 686 | 723 | 404 | 415 | --- | --- | --- |
| **Single crystal (RSA)** | 290 | 16 | < 10 | 19 | 48 | --- | --- | --- |
| **Single crystal (Pi-Kem)** | --- | 0.6 | 0.2 | 1.5 | 9 | 2.5 | 0.4 | 0.3 |

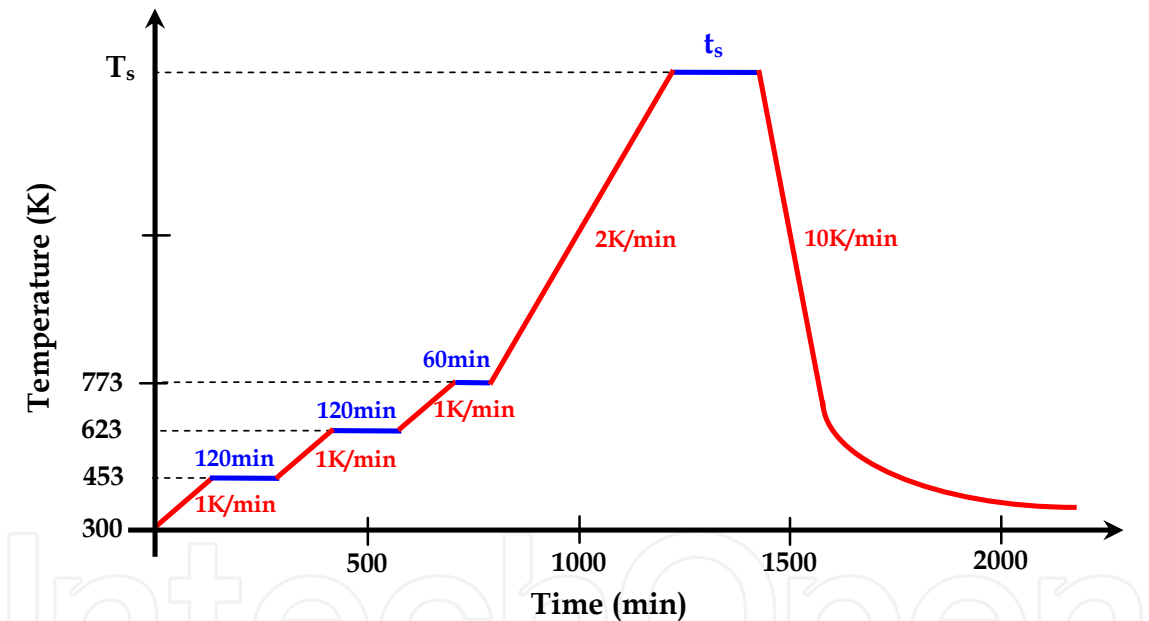Table 1. Composition of alumina materials (impurities in ppm).



Fig. 1. Schematic description of the firing schedule of the sintering process.

The grain diameters, d, and densities of the sintered samples, which were achieved via the control of the sintering temperature, $T_s$, and the dwelling time, $t_s$, are given in Table 2.

The grain sizes were determined by the intercept method. The sample surfaces were first polished and then thermally etched to reveal the grain boundaries. Etching was performed by holding the sample at 50 K below the sintering temperature $T_s$ (during 15 to 30 min) after a rapid heating. The average grain sizes were calculated from the values of 100 to 200 grain size measurements from Scanning Electron Microscope "SEM" images of the surface using different magnifications. Figure 2 shows, as example, the microstructure of the 1.2 μm grain diameter of the impure polycrystalline alumina sample.

|  | grain diameter, d (µm) | sintering temperature, $T_s$ (K) | dwelling time, $t_s$ (min) | density (in % of theoretical) |
|---|---|---|---|---|
| "pure" samples | 1.7 | 1863 | 100 | 98.7 |
|  | 2.7 | 1893 | 120 | 98.9 |
|  | 4.5 | 1923 | 120 | 99.1 |
| "impure" samples | 1.2 | 1773 | 180 | 95.7 |
|  | 2 | 1823 | 180 | 98 |
|  | 4 | 1923 | 360 | 95.4 |

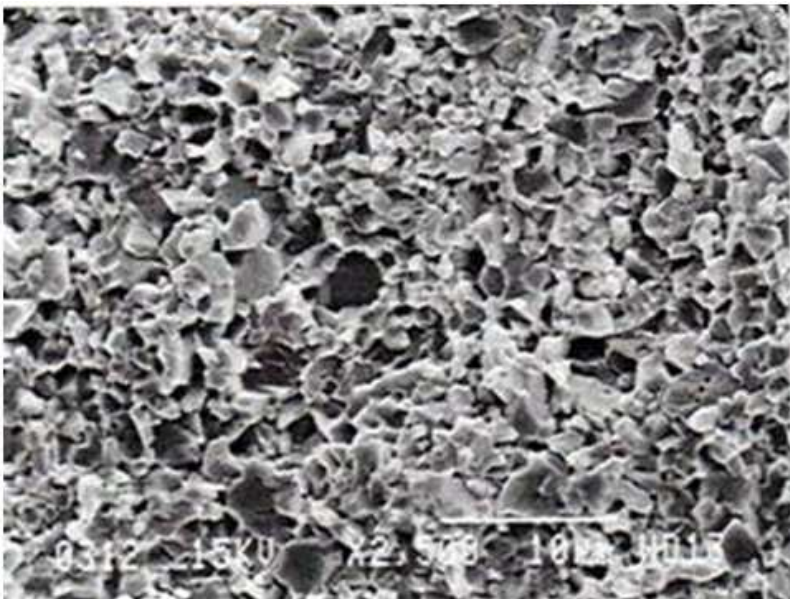Table 2. Sintering temperature, dwelling time at the sintering temperature and corresponding grain diameters and densities (Liebault, 1999).



Fig. 2. Microstructure of the 1.2 µm grain diameter of the impure polycrystalline alumina sample (SEM image).

## 3.2 Single crystals (as reference materials)

The single crystals are selected for the purpose of providing reference materials, which will be compared to the sintered alumina. Two types of single crystals taken from a Verneuil-grown rod are considered (Table 1). The first of very low impurity content (about 15 ppm) is provided by Pi-Kem Co. (U.K.). The second, manufactured by RSA Co. (France), contains about 380 ppm of various impurities (with 290 ppm of silicon). The samples were polished to flat mirror surface finishes, using successively finer grades of diamond pastes down to 1 µm. In order to anneal the defects induced by machining and polishing, a thermal treatment in air at 1773 K during 4 hours was performed.

### 3.3 Characterization of defects in sintered alumina using positron annihilation lifetime spectroscopy

In this section, complementary investigations concerning the use of Positron Annihilation Lifetime Spectroscopy "PALS" for the characterization of defects in alumina will be summarized (Moya et al., 2003; Si Ahmed et al., 2005). After a short description of the procedure, we will spotlight the results relevant to the charging properties.

#### 3.3.1 Experimental procedure

The positron lifetime spectra of the samples, identical to those described in Table 1, were recorded at room temperature using a conventional fast-fast coincidence system with γ detectors consisting of plastic scintillators characterized by a time resolution of 270 ps. The $^{22}$Na positron source, 10 μCi sealed by 0.75 μm thick nickel foils, was sandwiched between two identical samples (of 20 mm diameter and 2 mm thickness). The spectra were measured in 2000 channels, with a calibration of 27 ps/channel, collecting $6.9 \times 10^6$ to $20 \times 10^6$ counts.

#### 3.3.2 Spectra analysis

The experimental spectra were fitted via a LTV.9 program (Kansy, 1996), in which a three-state trapping model was introduced into the source code (Krause-Rehberg & Leipner, 1999).

In the case of single crystal Pi-Kem, the spectra analysis reduces to only one lifetime component ($\tau_b$ = 117 ± 1 ps) associated with reasonable confidence to annihilation in bulk free defects. The quite high intensity of this component, (98.4 ± 1.6) %, appears as an unequivocal justification of the absence of discernable defects that are able to trap positrons (e.g., dislocations, negatively charged vacancies, neutral complexes). This result is also interpreted as a confirmation of the very low impurity content, which therefore justifies its choice as reference material for assessing the effects of both the microstructure achieved by the sintering process and the impurity content. For the sintered samples, three lifetime components were deduced. The shortest lifetime ($\tau_b$ = 122 ± 4 ps) was attributed to annihilation in the bulk free defects as it is very close to the one of the reference material, the intermediate ($\tau_g$ = 137 ± 2 ps) to trapping in defects within the grains and the longest ($\tau_{gb}$ = 397 ± 22 ps) to trapping in clusters located at grain boundaries.

Since Silicon is the main impurity in sintered samples, the possible defects felt by positrons within the grains are isolated vacancies $V_{Al}'''$ and $(Si_{Al}^{\bullet}:V_{Al}''')''$, $(2Si_{Al}^{\bullet}:V_{Al}''')'$, $(3Si_{Al}^{\bullet}:V_{Al}''')^x$ clusters. However, the neutral cluster $(3Si_{Al}^{\bullet}:V_{Al}''')^x$ is more likely than the others due to the sintering temperatures and dwelling times (Lagerlöf & Grimes, 1998). In any case, the positron lifetime in all these defects is expected to have about the same value ($\tau_g$ = 137 ± 2 ps) because it is primarily determined by $V_{Al}'''$ (Moya et al., 2003). The nature of clusters at grain boundaries is more difficult to ascertain because of the competition between all impurities for the segregation sites. However, one can speculate that the lifetime of about 400 ps ($\tau_{gb}$ = 397 ± 22 ps) reflects positron trapping in neutral or negatively charged clusters of charge compensating native vacancies $V_{Al}'''$ and $V_O^{\bullet\bullet}$, which are induced by the impurities that have the strongest tendency for segregation, for instance $SiO_2$, MgO and CaO. In particular, $V_O^{\bullet\bullet}$ could stem from the dissolution of CaO (Eq. 5), which, incidentally displays by far the highest enrichment ratio, about 1300 (Dörre & Hübner, 1984).

## 4. Method for the characterization of the charging state of dielectrics

In insulator material, the charges can be injected through interfaces, via an applied voltage, or created by irradiation via energetic particles. For instance, incident electrons, as they slowdown, can generate pairs of electrons and holes. These charge carriers can recombine, be trapped or move as a result of diffusion and/or field conduction. Concurrently, some of the electrons can be emitted from the sample surface and a distribution of trapped charges may develop within the irradiated volume. In our case, experiments are carried out using the electron beam of a SEM. The experimental set up, described below, provides means for measuring the evolution of the net amount of trapped charges $Q_t$, which characterize the charging state of the insulator. For this purpose, we use the Induced Current Measurements "ICM" method (called also the Displacement Current Measurements), which we have recently improved (Zarbout et al., 2008, 2010).

### 4.1 Experimental set up

The experiments are performed using a SEM (LEO 440), which is specially equipped (Fig. 3) to inject a controlled amount of charges $Q_{inj}$ with appropriate conditions (energy of incident electrons, charge and current beam densities, temperature). The electron beam is monitored by a computer system allowing the control of the beam parameters:

- beam energy, $E_p$ (varying between 300 and 40000 eV),
- current beam intensity, $I_p$ (ranging from a few pA to several hundred nA, with the possibility of reaching a few μA),
- irradiated beam area of the sample (varying between a few nm when the beam is focused and few hundred μm when it is defocused).
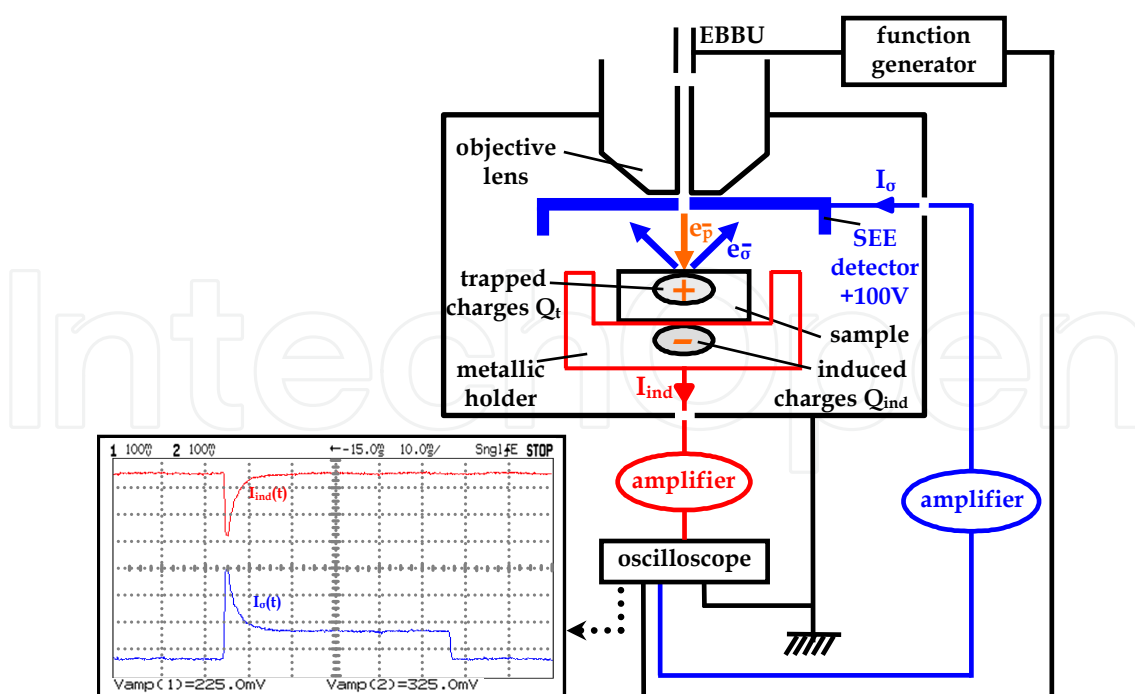


Fig. 3. Setting up for the measurement of the secondary electron current $I_\sigma$ and induced current $I_{ind}$. The secondary electron detector (diameter 15 cm) is positioned at a distance of about 2 cm from the sample surface.

Furthermore, the injection time, $t_{inj}$ (ranging from $10^{-3}$ to 1 s), is adjusted by the Electron Beam Blanking Unit "EBBU" using a function generator, allowing the turns off on the spot over the specimen surface with no electron track outside the investigated area when the beam is blanked.

The metallic sample holder is attached to a cooling-heating stage (temperature range 93 − 673 K). Hence, in situ thermal sample cleaning under vacuum (at T = 663 K during 180 minutes) and sample characterization at different temperatures are possible. Prior to electron irradiations, after the cooling that follows the cleaning step, the sample is held during 180 minutes at the testing temperature, so that the thermal equilibrium between the sample and the metallic holder is approached.

### 4.2 The improved Induced Current Measurement method

The ICM method is based on the measurement of the current $I_{ind}$, produced by the variation of the induced charges $Q_{ind}$ (in the sample holder) due to the trapped charges in the sample $Q_t$ (Liebault et al., 2001, 2003; Song et al., 1996). Since the influence coefficient in our experimental set up is close to one (Zarbout et al., 2008), the amount of the net trapped charges is given by:

$$Q_t(t) = -Q_{ind}(t) = -\int_0^t I_{ind}(t)\,dt \qquad (7)$$

The improvement brought to the ICM method consists in the concurrent measurement of $I_{ind}$ and the total secondary electron current $I_\sigma$ due to the sole electrons emitted by the sample. For this purpose, as shown in Fig. 3, the SEM is specially equipped with a secondary electron low-noise collector located under the objective lens just above the sample. A biased voltage of 100 V is applied to it in order to collect all the electrons escaping from the sample surface.

During charge injection, the currents, $I_\sigma$ and $I_{ind}$, are simultaneously amplified (Keithley 428) and observed on an oscilloscope (HP 54600B) where the material response is displayed after a short lag time. The primary current beam $I_p$ (which is adjusted in a Faraday cage) and the current $I_\sigma$ are always positive whereas $I_{ind}$ can be positive or negative depending on the Secondary Electron Emission "SEE" yield $\sigma$, which is equal to $I_\sigma/I_p$. Then if $I_\sigma$ is higher than $I_p$ ($\sigma > 1$), the sample charges positively and $I_{ind}$ is negative. In the other case ($\sigma < 1$), the sample charges negatively and $I_{ind}$ is positive. The general variation of $\sigma$ with $E_p$ is shown in Fig. 4.
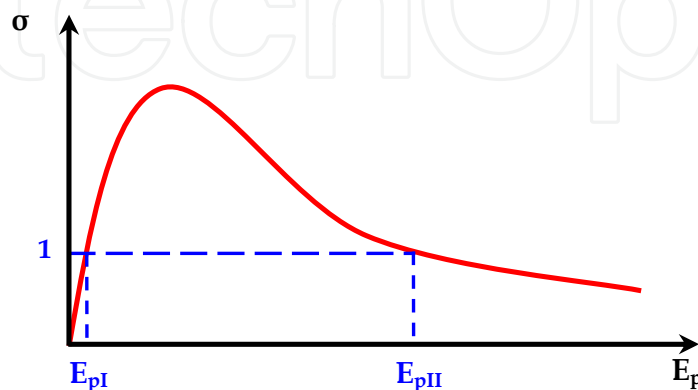


Fig. 4. Schematic evolution of the SEE yield σ with primary beam energy $E_p$ for uncharged insulator materials.

The sign of the net sample charges (i.e., net trapped charges) depends mainly, for a given material, on the primary beam energy $E_p$ and the primary current beam density J. In the case of α-alumina, a sign inversion of the net trapped charges is observed for J greater than $7 \times 10^6$ pA/cm$^2$ (Thome et al., 2004).

Experiments are performed with a 10 keV primary electron beam energy which is located, for the α-alumina materials, between the two crossover energies of primary electrons $E_{pI}$ and $E_{pII}$ (about 20 keV) for which σ is equal to 1. To probe a zone representative of the material we use a defocused beam over an area of 560 μm diameter Φ, which has been accurately measured using an electron resist (Zarbout et al., 2005). With the utilized value $I_p$ = 100 pA, the primary current beam density is J = $4 \times 10^4$ pA/cm$^2$. These experimental conditions give rise to net positive trapped charges (σ > 1) and then a negative induced current, as shown in the curves recorded by the oscilloscope in Fig. 3.

The positive surface potential developed by the trapped charges $Q_t$ does not exceed a few volts, which is very low to produce any disturbance of the incident electron beam and of the measurement process (Zarbout et al., 2008). Then, the good stability and reliability of the SEM ensure (for a biased voltage applied to the secondary electron collector greater than about 50 V) the current complementarity according to the Kirchhoff law:

$$I_p(t) = I_{ind}(t) + I_\sigma(t) \tag{8}$$

Hence, the presence of the collector with a sufficient biased voltage allows accurate measurements of the currents and therefore the precise determination of the quantity of trapped charges. Incidentally, this makes also possible a precise calculation of the SEE yield σ(t):

$$\sigma(t) = \frac{I_\sigma(t)}{I_p(t)} = \frac{I_p(t) - I_{ind}(t)}{I_{ind}(t) + I_\sigma(t)} = 1 - \frac{I_{ind}(t)}{I_{ind}(t) + I_\sigma(t)} \tag{9}$$

The SEE yield could be deduced directly from the secondary electron current $I_\sigma(t)$ and the primary one $I_p(t)$. However, the use of $I_\sigma(t)$ and $I_{ind}(t)$ in Eq. 9 is more appropriate as it provides the opportunity to circumvent any uncontrolled fluctuation of the primary electron current during the different phases of the experimental process.

It is worth noting that after the fabrication process of polycrystalline samples (with firing temperatures above 1863 K) or the thermal treatment of single crystals (at 1773 K for 4 hours), the final thermal cleaning stage under vacuum of all the samples prior to electron irradiation will completely remove initial charges and surface contamination that could interfere with the generated charges.

## 4.3 The charging kinetic

The measurement of the foregoing currents gives means to follow the net quantity of trapped charges during irradiation. The current curves $I_\sigma(t)$ and $I_{ind}(t)$ of Fig 5 are a typical example of the recorded currents. As pointed out in the experimental conditions, irradiation is performed with a 10 keV electron beam energy, which ensure a net amount of positive charges in the sample.
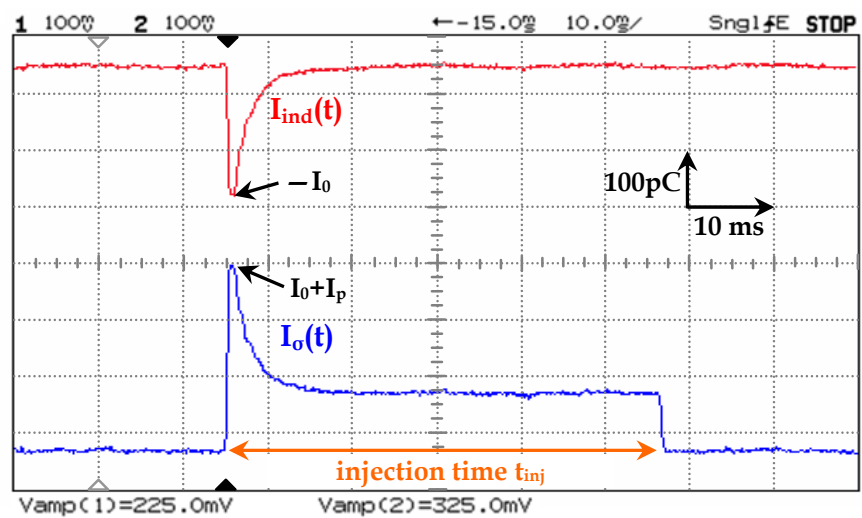
Fig. 5. Current curves recorded during the first injection in polycrystalline alumina sample ($d$ = 4.5 µm) at 473 K. The currents, $-I_0$ = $-$ 225 pA and $I_0 + I_p$ = 325 pA, are measured after a short lag time. The irradiation conditions are: $E_p$ = 10 keV, $I_p$ = 100 pA, $t_{inj}$ = 5 ms, $Q_{inj}$ = 5 pC and J = $4 \times 10^4$ pA/cm².

At the beginning of injection, the current curves are affected by the rise time of the amplifiers. Therefore, a short lag time is required to display the actual current values $-I_0$ and $I_0 + I_p$. As irradiation proceeds, the induced current, $I_{ind}$, increases from $-I_0$ to zero. Concurrently and since the current complementarity conditions are verified (as revealed by Eq. 8), the total secondary electron current $I_\sigma$ decreases from ($I_0 + I_p$) to $I_p$. This decrease has been associated with a progressive accumulation of positive charges that are distributed over a depth of about the escape length of secondary electrons $\lambda$. As suggested, this could be assigned to recombination of electrons with holes (in this zone), which should be otherwise emitted (Cazaux, 1986) or to field effect (Blaise et al., 2009). The other important feature is indeed that during injection, a negative charge distribution develops in the vicinity of the penetration depth of primary electrons $R_p$. As result, an internal electric field is established between the two charge distributions (holes near the surface and electrons around $R_p$) whose direction is oriented towards the bulk. Since the diameter $\Phi$ of the irradiated area is much larger than the penetration depth, a planar geometry can be used to evaluate this field (Aoufi & Damamme, 2008) from the Gauss theorem:

$$E(z,t) = \frac{-1}{\varepsilon_0 \varepsilon_r (1+\varepsilon_r)} \left( 1 + \frac{\Phi^2}{4(1+\varepsilon_r)e^2} \right)^{-1} \int_0^e \rho(z,t)dz + \frac{1}{\varepsilon_0 \varepsilon_r} \int_0^z \rho(z,t)dz \qquad (10)$$

In this expression, where the contribution of image charges has been taken into account, e is the sample thickness, $\varepsilon_0$ is the vacuum permittivity, $\varepsilon_r$ the relative permittivity (taken equal to 10 for α-alumina) and $\rho(z, t)$ is the density of charges at the depth z. The first term corresponds to the surface electric field E (0, t).

When $I_{ind}$ reaches a zero value ($I_\sigma(t) = I_p(t)$), a steady state, which corresponds in fact to a self regulated flow regime, is achieved. There, on the average, for each incident electron one secondary electron is emitted. This state is characterized by some constant value of the

electric field as well as by a maximum amount of net trapped charge in the sample, $Q_{st}$, equal to $-\int_0^{t_{inj}} I_{ind}(t)\,dt$. The steady state is interesting because it will be taken as a reference state and then the practical choice of the injection time $t_{inj}$ is determined by the achievement of this state. The evolution of the net trapped charges $Q_t$ during injection, which can be deduced from Eq. 7, is shown in Fig. 6.
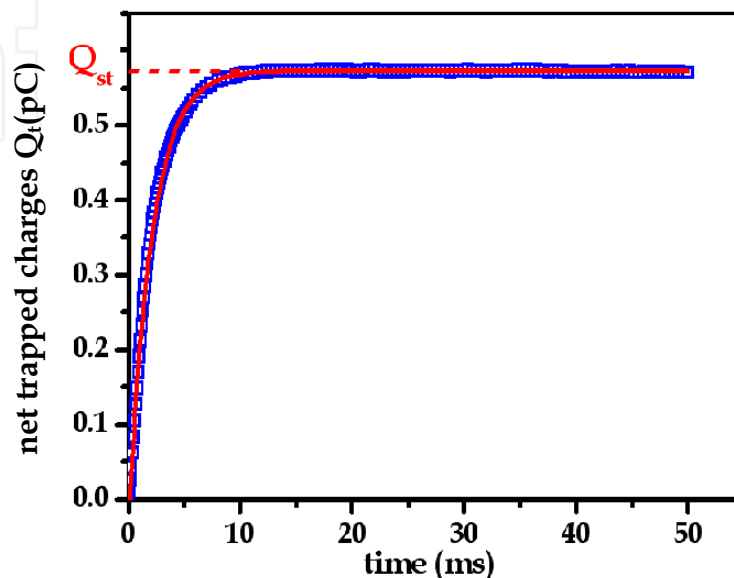


Fig. 6. Evolution with time, at 473 K, of the net charge, $Q_t$, during the first pulse injection in polycrystalline alumina sample (d = 4.5 μm). The quantity $Q_t$ is derived from the currents of Fig. 5 via Eq. 7. The solid line represents the exponential fit of the data, as given by Eq. 11.

The best fit of data represented in Fig. 6, leads to an exponential time evolution:

$$Q_t(t) = Q_{st}\left[1 - \exp\left(-\frac{t}{\tau_c}\right)\right] \qquad (11)$$

where $\tau_c$ is the charging time constant (found equal to $2.07 \times 10^{-3}$ s), which characterizes the charging kinetic of the material in the used experimental conditions.

## 5. Measurement of the ability to spread charges

The method described above gives the opportunity to evaluate the quantity of trapped charges during irradiation. If the probed zone is initially uncharged, $Q_t(t)$ characterizes the quantity of charges that accumulates after an irradiation time t. Depending on the insulator conduction properties, the accumulated charges can either remain localized or partially (or even totally) spread out of the irradiated volume (discharge phenomenon). Hence, the measurement of the ability of the material to spread charges is of technological interest. In this paragraph, we give details of the experimental procedure developed for the measurement of this ability and we define a recovery parameter allowing the quantitative evaluation of the extent of discharge.

### 5.1 Experimental protocol

To characterize the degree of spreading (of discharge), we set up a protocol allowing its evaluation. The procedure consists in analysing the states of charging deduced from two pulse electron injections over the same area, separated by some lapse of time as explained in the three following stages.

### 5.1.1 The first charging stage (first pulse injection)

The first stage is intended to achieve a charging reference state, which is attained once σ reaches the constant value of 1, i.e. the situation where for each electron entering one is emitted. This charging reference state is associated with the trapping of a maximum quantity of charges $Q_{st}$ (cf. Fig. 6). The embedded charges can be either indefinitely trapped or just localised for some time lapse (seconds, minutes, hours or more). If all the charges were trapped in a stable way, the foregoing reference state would stay unchanged when irradiation is turned off. In the case of partially localised charges, some fraction of $Q_{st}$ could manage to spread out from irradiated region, through conduction. To take into account this fact, a pause time long enough to appraise the degree of charge spreading is chosen for the pause stage.

### 5.1.2 The pause stage

During the pause time $\Delta t$, the stability of the amount of charges $Q_{st}$ is determined by the efficiency of traps associated with impurities and lattice defects as well as the charge transport properties. Then, if one wants to evaluate the extent of discharging, one has to perform, with identical conditions, a second injection over the same area as the first one for the purpose of restoring the reference steady state.

### 5.1.3 The third stage (second pulse injection)

At the inception of the second injection, if the recorded currents are in the continuity of those of the first injection, all the charge $Q_{st}$ have remained trapped in the irradiated volume during the pause time $\Delta t$. If it is not the case, a fraction of the charge $Q_{st}$ has been removed from the irradiated zone as a result of discharging (i.e., detrapping and transport) during the pause time.

For the purpose of illustration, the curves of Fig. 7 display the recorded currents during the second injection, performed over the same area as the first injection and with identical experimental conditions, after a pause time $\Delta t = 900$ s. Here, the current curves are not in the continuity of those obtained at the end of the first injection (Fig. 5). As the second injection proceeds, the reference steady state is reached again. The ensuing quantity of net charge introduced during this stage is interpreted as the amount $Q_d$ that has been removed, given by:

$$Q_d = \left[ -\int_0^{t_{inj}} I_{ind}(t)\, dt \right]_{second\ injection} \tag{12}$$

In other words, this interpretation means that any loss of charges, during the pause, can be compensated by those introduced during the second irradiation to restore $Q_{st}$.
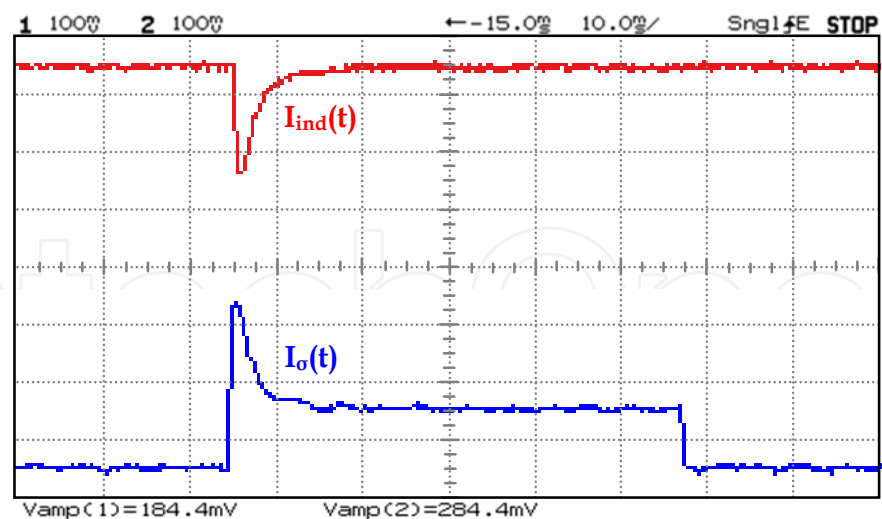
Fig. 7. Current curves obtained during the second pulse injection performed after a pause time Δt = 900 s. Irradiation is carried out over the same area as in the first injection under identical experimental conditions (given in Fig. 5).

The three stages are summarized in Fig. 8, which illustrates the evolution of the amounts of charges remaining in the irradiated volume in the polycrystalline sample of grain diameter d = 4.5 μm at T = 473 K. The data concern the example of Figs. 5 and 7, for which some discharging occurs during the pause Δt. During the pause time $t_p$ ($0 \le t_p \le \Delta t$), the net charge that still remains in the irradiated volume $Q_l(t_p)$ evolves from its initial value, $Q_l(t_p = 0) = Q_{st}$, to the final one, $Q_l(t_p = \Delta t) = Q_f$. The form of the curve representing $Q_l(t_p)$ will be justified below.
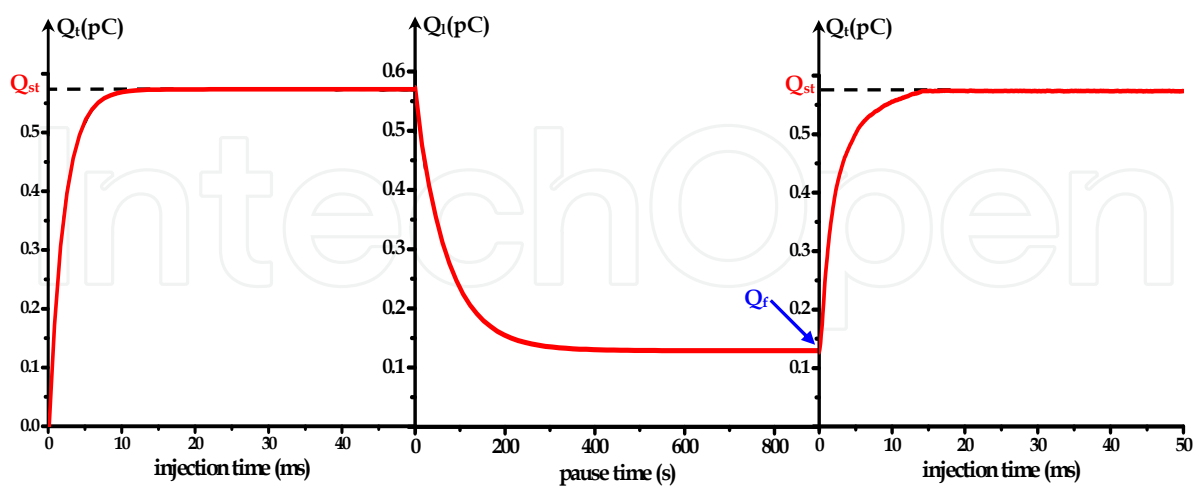


Fig. 8. Illustration of the time evolution of the amounts of charges remaining in the irradiated volume during the three stages. The first and the third curves correspond to Figs. 5 and 7 respectively. The net charge $Q_l(t_p)$ during the pause evolves from $Q_{st}$ to $Q_f$ (which remains in the irradiated volume after a pause of Δt =900 s) as justified below by Eq. (15).

## 5.2 Definition of a recovery parameter for the evaluation of discharge

We first try to find a kinetic description of the charges that remain in the irradiated volume after a pause time $t_p$. This amount is given by:

$$Q_l(t_p) = Q_{st} - Q_d(t_p) \tag{13}$$

where, $Q_d(t_p)$ is given by Eq. 12.

As an example, in Fig. 9, we report the best fit of the evolution of $Q_d$ with $t_p$, for data obtained, at 473 K in polycrystalline alumina sample (d = 4.5 µm), by performing the measurements over different zones that are sufficiently distant from one another to avoid any overlaps of irradiated volumes.

The fit is well described by an exponential with a time constant $\tau_r$:

$$Q_d(t_p, T) = Q_\infty(T) \left[ 1 - \exp\left( -\frac{t_p}{\tau_r(T)} \right) \right] \tag{14}$$

In this equation, $Q_\infty$ is the asymptotic value reached by $Q_d$. In fact, it stands for the maximum amount of charges going out of the irradiated volume in the discharging process at temperature T. In the example of Fig. 9 where T = 473 K, $Q_\infty$ is found equal 0.46 pC corresponding to about 80 % of $Q_{st}$ (hence, 20 % of the net charge is still inside the irradiated volume). This is an indication of the existence of different trapping sites and that the temperature of 473 K is too low to provoke detrapping from the deeper ones.
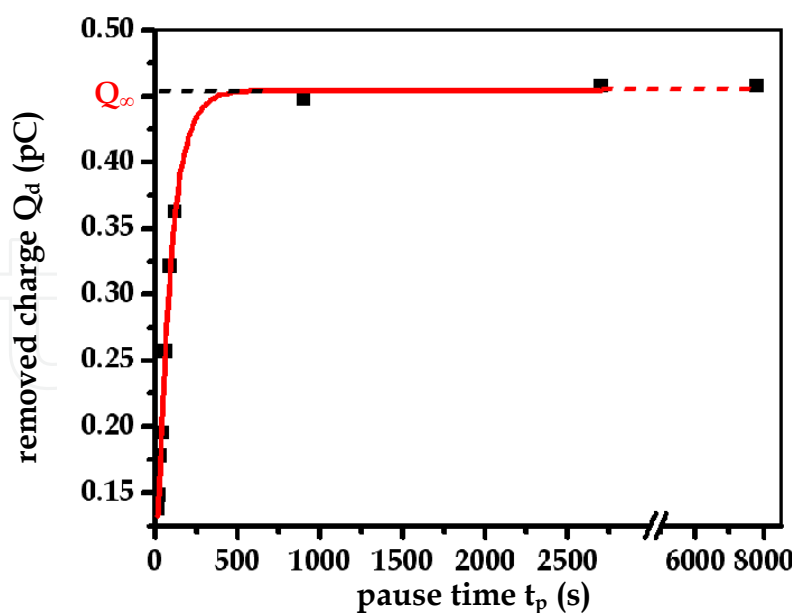


Fig. 9. Evolution with the pause time at T = 473 K of the amount of charges that is removed from the irradiated volume $Q_d$ (in polycrystalline sample of 4.5 µm grain size). The solid line is the exponential fit of the data (Eq. 14). The asymptotic value $Q_\infty(T)$ is attained after a pause time of only 300 s.

From Eq. 14, we can associate to $Q_\infty(T)$ the amount of charges $Q_f(T)$ that still remain in the irradiated volume, $Q_\infty(T) = Q_{st} - Q_f(T)$. Therefore, the remaining quantity of charges $Q_l(t_p, T)$ can be obtained from Eqs. 13 and 14:

$$Q_l(t_p, T) = (Q_{st} - Q_f(T)) \exp\left(-\frac{t_p}{\tau_r(T)}\right) + Q_f(T) \tag{15}$$

The first term in this expression, which corresponds to the curve of the pause stage in Fig. 8, expresses charge decay under the internal electric field. Generally, the time constant $\tau_r$ can be set equal to $\varepsilon/\gamma$, where $\varepsilon$ is the dielectric permittivity ($\varepsilon = \varepsilon_r \varepsilon_0$) and $\gamma$ is the electric conductivity of the material (Adamiak, 2003; Cazaux, 2004). The value of $\tau_r$ deduced from Fig. 9 is 82 s giving a conductivity of about $10^{-14}$ $\Omega^{-1}cm^{-1}$ which can be expected for this material, in agreement with the experimental value of the resistivity obtained for this sample in our laboratory (1.2 $10^{14}$ $\Omega cm$).

The asymptotic value $Q_\infty$ at T = 473 K is reached after only 300 s (Fig. 9). Therefore, one can anticipate that at temperatures within the range of interest (300 − 663 K), the condition for reaching the asymptotic value $Q_\infty(T)$ are met for the chosen pause time $\Delta t$ of 900 s.

The measured value of $Q_\infty(T)$ is the result of detrapping of charges and their subsequent transport under the internal electric field. During this transport, a fraction of the detrapped charges can undergo a retrapping in deeper traps in the irradiated volume and eventually a recombination. The overall effect is a variation of charge distribution in the volume of interest, which affects the electric field. Consequently, since in the considered temperature range the experimental results do not reveal any significant dependence of $Q_{st}$ on temperature, the ratio $R(T) = Q_\infty(T)/Q_{st}$ can be expressed in terms of the measured currents:

$$R(T) = \frac{Q_\infty(T)}{Q_{st}} = \frac{-\left[\int_0^{t_{inj}} I_{ind}(t)dt\right]_{second\ injection}}{-\left[\int_0^{t_{inj}} I_{ind}(t)dt\right]_{first\ injection}} \tag{16}$$

This experimental parameter, which measures the fraction of charge removed from the irradiated volume, also characterizes the extent of discharging.

The ratio R(T), which can vary between 0 and 1, corresponds to an evolution from either the dominance of stable charge trapping (low values of R) or of charge spreading (high values of R, with R = 1 for a complete recovery of the uncharged state). The rate at which charges are detrapped depends usually on an attempt escape frequency and an activation energy linked to the trap depth. As a result, one can expect that, the variation of R with temperature could shed some light on the discharge process.

## 6. Effect of microstructure induced by sintering on the ability of a dielectric to trap or spread charges

As it will be pointed out, trapping and spreading are intimately linked to the microstructure and defects. Sintering not only leads to the creation of new interfaces but also to important phenomena such as segregation at grain boundaries and defects association.

## 6.1 Charge spreading in reference materials (single crystals)

The results of the two types of single crystals are reported in Fig. 10. The values of R in both Pi-Kem and RSA are zero up to 473 K, indicating a perfect stable trapping behavior. Above 473 K, R increases but the enhancement is significant only for Pi-Kem.
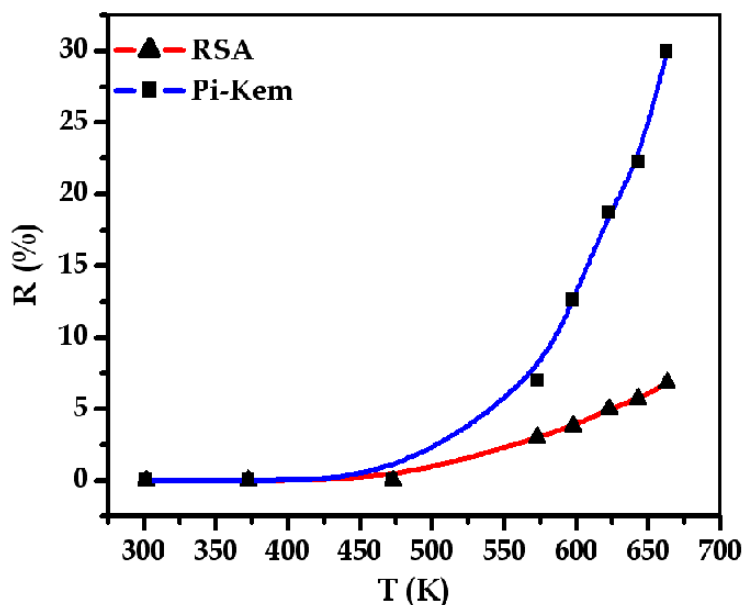


Fig. 10. Fraction R of charges removed from the irradiated volume as a function of temperature for the two types of single crystals (Pi-Kem and RSA samples).

In order to interpret these behaviors we can consider the following results:

i.    Cathodoluminescence spectra obtained in similar Pi-Kem samples (Jardin et al., 1995) have identified mainly the F and F+ centers. Stable trapping in these centers is expected due to their deep level in the band gap (3 eV, and 3.8 eV for the F and F+, respectively). The increase of R above 473 K might be due to the intervention of excited F centers whose energy levels are believed very near the edge of the conduction band (Bonnelle & Jonnard, 2010; Jonnard et al. 2000; Kröger, 1984).
ii.   The RSA material displays a more stable trapping ability than the Pi-Kem one above 473 K. This stable trapping raises queries about the role of the defects induced by the impurities (Table 1) and in particular those by the dominant silicon. With such amount of silicon (290 ppm), the concentration of the defects associated with Si exceeds the others. Consequently, one can deduce that stable trapping may occur on these defects.

As mentioned in paragraph 2, the dissolution of silicon into $Al_2O_3$, is expected to be compensated by a negatively charged cationic vacancy, $V_{Al}^{'''}$ (Eq. 4). In this context, the positively charged substitutional silicon $Si_{Al}^{\bullet}$ may act as electron trapping site while the cationic vacancy $V_{Al}^{'''}$ as hole trap. Upon trapping one electron during irradiation, $Si_{Al}^{\bullet}$ induces a donor level associated to $Si_{Al}^{\times}$, which is estimated at 1.59 eV below the edge of the conduction band (Kröger, 1984). With regard to $V_{Al}^{'''}$, hole trapping will give an acceptor level (associated to $V_{Al}^{''}$) located at 1.5 eV above the valence band (Kröger, 1984).

Accordingly, with such relatively deep trap levels, it is very unlikely that detrapping of charge carriers occurs at the temperatures of our experiments. However, the contribution of the other impurities, such as the ones of smaller valence than the host, cannot be ruled out because trapping depends not only on the defect concentration but also on their specific trapping properties such as the capture cross section of traps which is mainly determined by their charge state. Indeed, the cathodoluminescence spectra have also detected (Jardin et al., 1995) in similar RSA samples (which like ours were annealed at 1773 K during 4 hours) the deep centers $F_{cation}$, such as $F_{Mg}^{x}$ with an energy level at 4 eV below the edge of the conduction band (Kröger, 1984).

We alternatively tried to shed some more light on the trapping behaviors of single crystals by using the Scanning Electron Microscope Mirror Effect "SEMME" method, which requires net negative charging (Liebault et al., 2003; Vallayer et al. 1999). Thus, we performed electron injection with 30 keV (energy greater than $E_{pII}$) focused beam and an injected dose of 300 pC followed by a scanning of the sample surface, with low electron beam energy (some hundred of eV). In RSA samples we find a mirror image at 300 K, which remains stable up to about 663 K. In contrast, in Pi-Kem materials no mirror image formation was achievable even at 300 K.

It must be reminded that in the SEMME method the observation of a mirror image, immediately after irradiation, is due to the presence of a sufficiently high concentration of stable traps for electrons. Thus, no mirror image is observed in Pi-Kem samples as they do not contain enough traps. The fact that in RSA the mirror is maintained at high temperatures confirms the presence of deep traps and somewhat supports the assumption, discussed above in point (ii), that stable trapping can be assigned to the defects induced by the dissolution of the dominant silicon impurity.

In contrast with SEMME method, the ICM method can give, during charging, an induced current whatever the trap concentration is. So, the parameter R gives indications on the stability of trapped charges, after a pause $\Delta t$, independently of the trap concentration. As a result, at temperatures lower than 573 K, for which trapped charges are stable in RSA and Pi-Kem samples, the R values are very low (R = 0 at room temperature for both kinds of single crystals). Above 573 K, RSA samples have R values lower than those of Pi-Kem. This is a supplementary indication of the existence of deeper traps in RSA, which is one of the requirements for the mirror image formation at high temperatures in the SEMME method.

## 6.2 Charge spreading in sintered alumina of various microstructures and impurities

### 6.2.1 Charge spreading in pure sintered alumina

The values of R(T) for the three polycrystalline alumina pure samples as function of temperature are shown in Fig. 11. The comparison with single crystals (R close to zero up to 573 K) indicates that the presence of grain boundaries makes trapping less stable in polycrystalline alumina (R is substantially above zero). This interpretation agrees with the fact that, with SEMME method, we do not detect any mirror image in the polycrystalline samples.
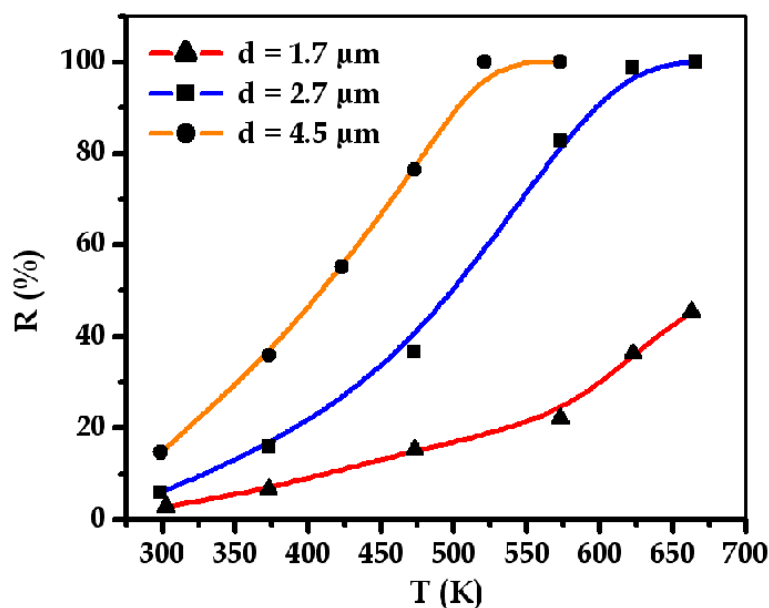
Fig. 11. Fraction R of charges removed from the irradiated volume as function of temperature for pure polycrystalline alumina samples of different grain diameters d.

In the RSA single crystal and pure polycrystalline alumina, silicon is the dominant impurity. Therefore, one can suggest that atomic disorder introduced by grain boundaries gives rise to states closer to the edge of the conduction band than those of $Si_{Al}^{\times}$ and $V_{Al}^{'''}$, which are most likely responsible for the stable trapping in the bulk.

For fine grains (d = 1.7 µm), R spans from 0 (at 300 K) to 45 % (at 663 K) whereas for large grains (d = 4.5 µm) R varies between 15 % (at 300 K) to near complete discharge (about 100 %) above 473 K. One would expect the behaviour of polycrystalline material to tend towards that of single crystals when the grain size increases. However, the reverse is clearly seen. The explanation of this apparent contradiction can be found by considering the distribution of impurities in the polycrystalline samples. We have to bear in mind that the microstructural evolution during the sintering process, with in particular the achievement of a given grain size, is concomitant with segregation to grain boundaries of impurities, which corresponds to a purification of the grain (interpreted as an internal gettering). In fact, the large grain size of 4.5 µm has required both a higher sintering temperature and a longer dwelling time than those used to attain 1.7 µm. Hence, the enhancement of gettering effect in large grain sample may have lowered the concentration of deep traps (such as $Si_{Al}^{\times}$ and $V_{Al}^{'''}$) in the bulk. In this assumption, the impurities (mainly Si) segregates at grain boundaries where they can be associated to other defects to form clusters, as suggested by positron measurements (cf. paragraph 3), which may be less efficient in trapping charges.

This agrees with the experimental facts:

i.   The R values are always higher for the larger grain (for example at 573 K, R = 100 % for d = 4.5 µm and only 22 % for d = 1.7 µm). This means that the density of deep traps in large grains is substantially lower.

ii.  The foregoing assumption is somewhat confirmed in Fig. 12, where below 573 K the semi-logarithmic plot of R versus reciprocal temperature exhibits an Arrhenius law leading to an activation energy about 0.12 eV whatever the grain size is. This same activation energy means that we are dealing with detrapping from similar trapping sites (i.e., grain boundary traps). The continuous variation in R over a large temperature range, as shown in Fig 11, indicates a detrapping from a density of continuous trapping states rather than from a single trapping level. This aspect characterizes disordered solids in which hopping conduction mechanism can occur with the same order of magnitude of activation energy (Blaise, 2001).
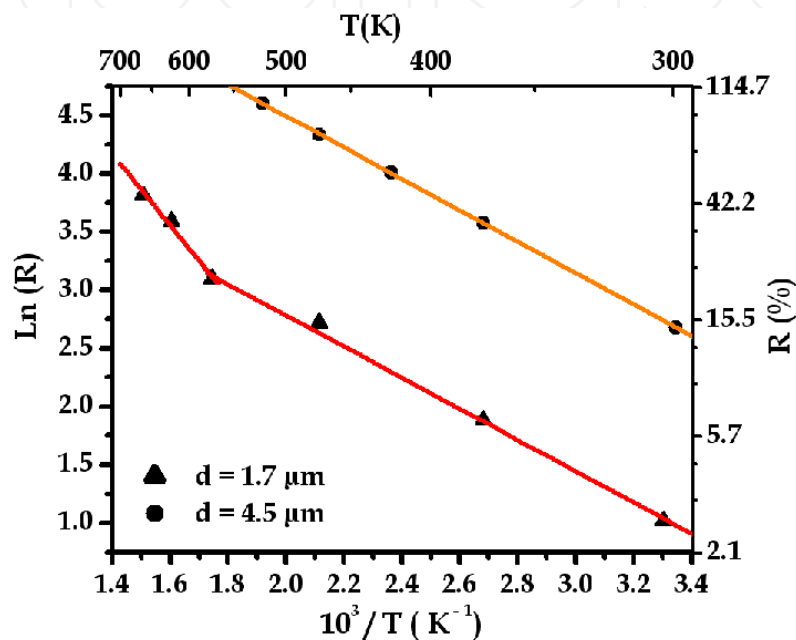


Fig. 12. Semi-logarithmic plot of the ratio R expressing the degree of discharge versus reciprocal temperature for polycrystalline alumina (solid line: linear fit of the data). For T below 573 K, discharging is characterized by the same activation energy (0.12 eV). Above 573 K, a second energy (0.26 eV) in small grains sample arises.

iii.  for temperature above 573 K the smallest grain size sample presents a second detrapping zone corresponding to an activation energy of about 0.26 eV (i.e., twice the energy at lower temperature). This fact is a further confirmation of the presence in the smaller grain size of a higher density of deeper traps located within the grain (likely $Si_{Al}^{\times}$ and $V_{Al}^{'''}$) in accordance with a less efficient gettering effect.

### 6.2.2 Charge spreading in impure sintered alumina

The results of the three polycrystalline alumina impure samples are reported in Fig. 13. The comparison of the pure and impure polycrystalline samples reveals a more stable trapping behavior in impure samples in the whole temperature range. Furthermore, two opposite behaviors arise: stable trapping increases with the grain diameter in impure samples (Fig.13) and the contrary is obtained in the pure ones (Fig. 11). In the impure material, the contents of impurities are much higher and expected above the solubility limits. Hence, gettering

might be less efficient due to a possible saturation of grain boundaries. In addition, interactions between the various defects generated by the foreign elements are expected (Gavrilov et al., 1999). It must be pointed out that the great variety of impurities and their substantial content make difficult the interpretation of the results due to a possible interference of co-segregation, which is difficult to predict when more than three elements are involved. The actual situation is even more complicated by the fact that segregation leads to the creation of a space charge at grain boundaries (Tiku & Kröger, 1980) with a sign that depends on the segregated impurities, which may interfere with the charging process.
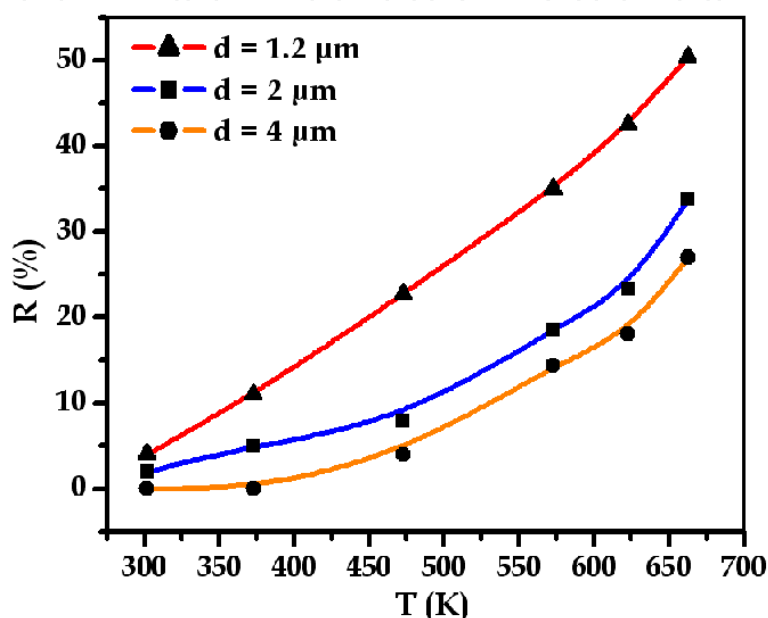
Fig. 13. Fraction R of charges removed from the irradiated volume as a function of temperature for impure polycrystalline alumina samples of different grain diameters d.

The semi-logarithmic plot of the degree of discharge R versus reciprocal temperature exhibits, as for the pure samples, an Arrhenius type law leading to an activation energy of about 0.12 eV for the smallest grain size sample (d = 1.2 μm) and about 0.28 eV for the largest one (d = 4 μm). These activation energies are an indication of detrapping from trapping sites located within the grain boundary.

It is worth noting that, at room temperature and in the same impure polycrystalline samples, breakdown strength increases with the grain sizes (Liebault, 1999; Si Ahmed et al., 2005), which is also the case for the fraction of removed charges R. Therefore this correlation confirms the importance of charge spreading to prevent breakdown.

## 6.3 Charge spreading in alumina of sub-micrometric grain size

The evolution of the properties with the grain size raises queries about the effect of changing the grain size from micron to nanometer scales. The study of charging properties of nanostructured alumina is beyond the scope of the present chapter. However, there is interest in trying to verify whether they can be obtained by simple extrapolation from the results of micrometric grain size materials.

Nanopowders, with grain diameter of about 27 nm, have been synthesized by the gaseous phase method and compacted via magnetic compaction process at Ural State Technical University, Russia (Kortov et al., 2008). Next, sintering of the compacts has been carried out at Institut National des Sciences Appliquées (INSA) of Lyon (France). The sintering temperature of 1473 K (dwelling time 60 min) was reached at a rate of 3 K/min. As expected, with such heating rate, a substantial grain growth occurred (i.e., from 27 to about 100 nm, cf. Fig. 14). Indeed, grain growth could have been reduced by using faster heating rates that are made possible by different sintering techniques such as spark plasma sintering.
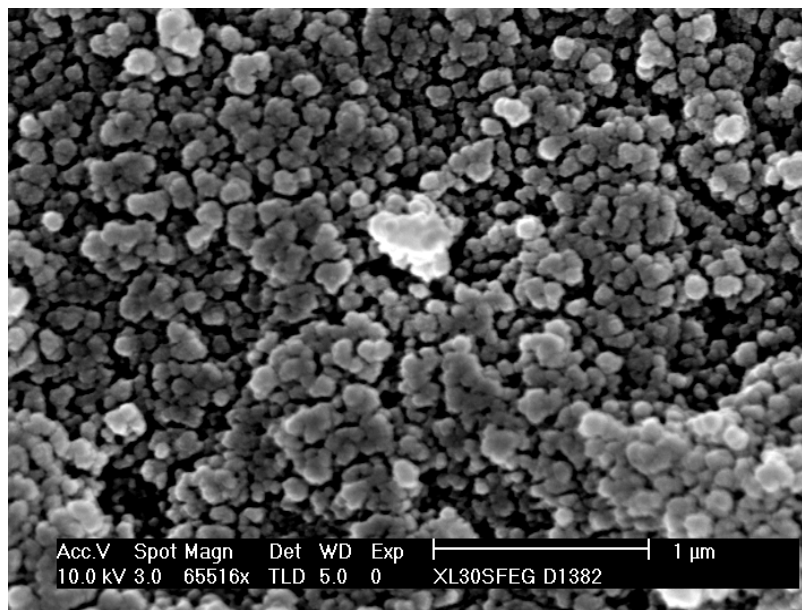


Fig. 14. Microstructure of the sub-micrometric grain size of the impure polycrystalline alumina sample after sintering. This picture is the SEM observation of fracture surface. The average grain diameter has grown after sintering to about of 100 nm (the initial particle diameter prior to sintering was about 27 nm).

The overall purity of this material is about the same as the one of impure polycrystalline alumina. In Fig. 15, the fraction R of charges removed from the irradiated volume as a function of temperature is given for the 0.1 and 1.2 μm samples. The manifest difference is the sharp enhancement of R between 600 and 663 K for the 0.1 μm sample (the value of R increases from 30 to 90 %), which contrasts with the continuous behaviour of the other polycrystalline samples. The activation energy that arises from the semi-logarithmic plot of the recovery parameter versus reciprocal temperature in the range 600-663 K is 0.53 eV (Moya et al., 2007). These results are an indication that detrapping occurs, at about 600 K, from a dominant efficient trap having a well-defined energy level in the gap as in the case of silver doped single crystal (Zarbout et al. 2010).
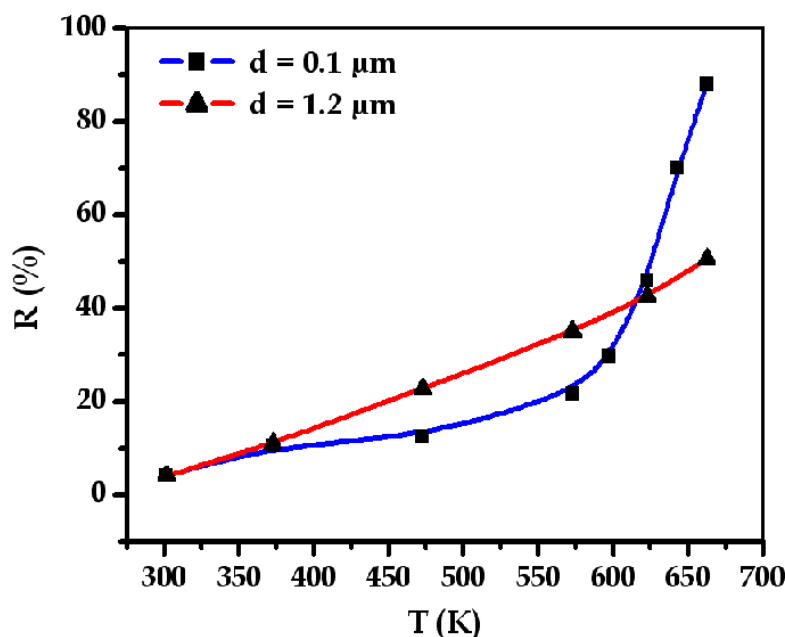
Fig. 15. Fraction R of charges removed from the irradiated volume as a function of temperature for the sub-micrometric and 1.2 μm grain sizes alumina samples.

## 7. Conclusion

This chapter provides a method for the characterization of charge trapping and spreading in dielectrics. A quantitative recovery parameters reflecting the relative degree of the two competing processes is accurately derived. The experimental set up makes possible the assessment of the effect of temperature (in the range 300-700 K). The ability of polycrystalline alumina to trap or, conversely, to spread charges depends strongly on the grain size and segregation of impurities at interfaces. The results suggest that the grain boundary interfaces can be associated to shallow traps whereas the defects within the grains to deeper ones. The strong tendency for segregation of the main impurities implies that an internal gettering effect can also intervene. It appears therefore that the control of the microstructural development, during the conventional sintering process, is of importance as it provides ways to influence the insulator properties in technological applications of oxide ceramics, for instance, the breakdown strength. Further investigations dealing with the properties of nanostructured materials, processed by sintering techniques that reduce grain growth, could bring more understanding of the role of interfaces.

## 8. Acknowledgments

## 9. References

Adamiak, K. (2003). Analysis of charge transport in high resistivity conductors under different conduction models. *Journal of Electrostatics*, Vol. 57, No. 3-4, (March 2003), pp. 325-335, ISSN 0304-3886

Aoufi, A. & Damamme, G. (2008). Analysis and numerical simulation of secondary electron emission of an insulator submitted to an electron beam. *Proceedings of ISDEIV 2008 23th International Symposium on Discharges and Electrical Insulation in Vacuum*, pp. 21-24, ISBN 978-973-755-382-9, Bucharest, Romania, September 15–19, 2008

Atkinson, K. J. W.; Grimes, R. W.; Levy, M. R.; Coull, Z. L. & English, T. (2003). Accommodation of impurities in $\alpha$-$Al_2O_3$, $\alpha$-$Cr_2O_3$ and $\alpha$-$Fe_2O_3$. *Journal of the European Ceramic Society*, Vol. 23, No. 16, (December 2003), pp. 3059-3070, ISSN 0955-2219

Blaise, G. & Le Gressus, C. (1991). Charging and flashover induced by surface polarization relaxation process. *Journal of Applied Physics*, Vol. 69, No. 9, (May 1991), pp. 6334-6339, ISSN 0021-8979

Blaise, G. (2001). Charge localization and transport in disordered dielectric materials. *Journal of Electrostatics*, Vol. 50, No. 2, (January 2001), pp. 69-89, ISSN 0304-3886

Blaise, G.; Pesty, F.; & Garoche, P. (2009). The secondary electron emission yield of muscovite mica: Charging kinetics and current density effects. *Journal of Applied Physics*, Vol. 105, No. 3, (February 2009), pp. 034101(1-12), ISSN 0021-8979

Bonnelle C. & Jonnard P. (2010). Dynamics of charge trapping by electron-irradiated alumina. *Physical Review B.*, Vol. 82, No. 7, (August 2010), pp. 075132(1-8), ISSN 1098-0121

Cazaux, J. (1986). Some considerations on the electric field induced in insulators by electron bombardment. *Journal of Applied Physics*, Vol. 59, No. 5, (March 1986), pp. 1413-1430, ISSN 0021-8979

Cazaux, J. (2004). Charging in Scanning Electron Microscopy "from Inside and Outside". *Scanning*, Vol. 26, No. 4, (July/August 2004), pp. 181-203, ISSN 1932-8745

Chiang, Y. -M.; Birnie III, D. & Kingery, W. D. (1996). *Physical Ceramics: Principles for Ceramic Science and Engineering*, (Wiley), John Wiley & Sons, ISBN 0-471-59873-9, New York

Dörre, E. & Hübner, H. (1984). *Alumina: processing, properties, and applications*, Springer-Verlag, ISBN 3-540-13576-6, Berlin

Gavrilov, K. L.; Bennison, S. J.; Mikeska, K. R. & Levy-Setti, R. (1999). Grain boundary chemistry of alumina by high-resolution imaging SIMS. *Acta Materialia*, Vol. 47, No. 15-16, (November 1999), pp. 4031-4039, ISSN 1359-6454

Gontier-Moya, E. G.; Bernardini, J. & Moya, F. (2001). Silver and Platinum diffusion in alumina single crystals. *Acta Materialia*, Vol. 49, No. 4, (autumn 2001), pp. 637-644, ISSN 1359-6454

Haddour, L.; Mesrati, N.; Goeuriot, D. & Tréheux, D. (2009). Relationships between microstructure, mechanical and dielectric properties of different alumina materials. *Journal of the European Ceramic Society*, Vol. 29, No. 13, (October 2009), pp. 2747-2756, ISSN 0955-2219

Jardin, C.; Durupt, P.; Bigarre, J. & Le Gressus, C. (1995). The surface potential and defects of insulating materials probed by electron and photon emissions. *Annual Report Conference on Electrical Insulation and Dielectric Phenomena*, pp. 548-551, ISBN 0-7803-2931-7, Virgina Beach, VA, USA, October 22-25, 1995

Jonnard, P.; Bonnelle, C.; Blaise, G.; Remond, G. & Roques-Carmes, C. (2000). F$^+$ and F centers in α-Al$_2$O$_3$ by electron-induced x-ray emission spectroscopy and cathodoluminescence. *Journal of Applied Physics*, Vol. 88, No. 11, (December 2000), pp. 6413-6417, ISSN 0021-8979

Kansy, J. (1996). Microcomputer program for analysis of positron annihilation lifetime Spectra. *Nuclear Instruments and Methods in Physics Research Section A: Accelerators, Spectrometers, Detectors and Associated Equipment*, Vol. 374, No. 2, (May 1996), pp. 235-244, ISSN 0168-9002

Kolk, J. & Heasell, E. L. (1980). A study of charge trapping in the Al-Al$_2$O$_3$-Si, MIS system. *Solid State Electron*, Vol. 23, No. 2, (February 1980), pp. 101-107, ISSN 0038-1101

Kortov, V. S.; Ermakov, A. E.; Zatsepin, A. F. & Nikiforov S. V. (2008). Luminescence properties of nanostructured alumina ceramic. *Radiation Measurements*, Vol. 43, No. 2-6, (February-June 2008), pp. 341 – 344, ISSN 1350-4487

Krause-Rehberg, R. & Leipner, H. S. (1999). *Positron Annihilation in Semi-conductors: defect studies*, Springer-Verlag, ISBN 3-540-64371-0, Berlin

Kröger, F. A. (1984). Electrical properties of α-Al$_2$O$_3$, In: *Advances in Ceramics, Vol. 10: Structure and Properties of MgO and Al$_2$O$_3$ Ceramics*, W. D. Kingery, pp. 1-15, American Ceramic Society, ISBN 0916094626, Columbus, OH

Lagerlöf, K. P. D. & Grimes, R. W. (1998). The defect chemistry of sapphire (α-Al$_2$O$_3$). *Acta Materialia*, Vol. 46, No. 16, (October 1998), pp. 5689-5700, ISSN 1359-6454.

Le Gressus, C.; Valin, F.; Henriot, M.; Gautier, M.; Duraud, J. P.; Sudarshan, T. S.; Bommakanti, R. G. & Blaise G. (1991). Flashover in wide-band-gap high-purity insulators: Methodology and mechanisms. *Journal of Applied Physics*, Vol. 69, No. 9, (May 1991), pp. 6325-6333, ISSN 0021-8979

Liebault, J. (1999). Ph. D. thesis. *Behavior of alumina materials during injection of charges. Relation between microstructure, dielectric breakdown and image current measurement (The SEMM method)*, Ecole Nationale Supérieure des Mines de Saint Etienne, France, INIST T 126061

Liebault, J.; Vallayer, J.; Goeuriot, D.; Tréheux, D. & Thévenot, F. (2001). How the trapping of charges can explain the dielectric breakdown performance of alumina ceramics. *Journal of the European Ceramic Society*, Vol. 21, No. 3, (March 2010), pp. 389-397, ISSN 0955-2219

Liebault, J.; Zarbout, K.; Moya, G. & Kallel A. (2003). Advanced measurement techniques of space-charge induced by an electron beam irradiation in thin dielectric layers. *Journal of Non-Crystalline Solids*, Vol. 322, No. 1-3, (July 2003), pp. 213-218, ISSN 0022-3093

Mohapatra, S. K. & Kröger, F. A., (1977). Defect structure of α-Al$_2$O$_3$ doped with titanium. *Journal of the American Ceramic Society*, Vol. 60, No. 9-10, (September 1977), pp. 381–387, ISSN 1551-2916

Moya, G. & Blaise, G. (1998). Charge trapping-detrapping induced thermodynamic relaxation processes, In: *Space Charge in Solids Dielectrics*, J.C. Fothergill & L.A. Dissado, pp. 19-28, Dielectric Society, ISBN 0 9533538 0 X, Leicester, UK

Moya, G.; Kansy, J.; Si Ahmed, A.; Liebault, J.; Moya F. & Gœuriot, D. (2003). Positron lifetime measurements in sintered alumina. *Physica Status Solidi (a)*, Vol. 198, No. 1, (July 2003), pp. 215-223, ISSN 1862-6319

Moya, G.; Zarbout, K.; Si Ahmed, A.; Bernardini, J.; Damamme, G. & Kortov, V. (2007). Grain size effect on electron transport properties of poly and nano-crystalline alumina, *First International Meeting on Nano-materials,* Belfast, January 13-15, 2007

Rasmussen, J. J. & Kingery, W. D., (1970). Effect of dopants on the defect structure of single-crystal aluminium oxide. *Journal of the American Ceramic Society*, Vol. 53, No. 8, (August 1970), pp. 436–440, ISSN 1551-2916

Si Ahmed, A.; Kansy, J.; Zarbout, K.; Moya, G.; Liebault, J. & Goeuriot, D. (2005). Microstructural origin of the dielectric breakdown strength in alumina: A study by positron lifetime spectroscopy. *Journal of the European Ceramic Society,* Vol. 25, No. 12, (2005), pp. 2813-2816, ISSN 0955-2219

Song, Z. G.; Ong, C. K. & Gong, H. (1996). A time-resolved current method for the investigation of charging ability of insulators under electron beam irradiation. *Journal of Applied Physics*, Vol. 79, No. 9, (May 1996), pp. 7123-7128, ISSN 0021-8979

Stoneham, A. M. (1997). Electronic and defect processes in oxides. The polaron in action. *IEEE Transactions on Dielectrics and Electrical Insulation*, Vol. 4, No. 5 (October 1997), pp. 604-613, ISSN 1070-9878

Suharyanto, Yamano, Y.; Kobayashi, S.; Michizono, S. & Saito, Y. (2006). Secondary electron emission and surface charging evaluation of alumina ceramics and sapphire. *IEEE Transactions on Dielectrics and Electrical Insulation*, Vol. 13, No. 1 (February 2006), pp. 72-78, ISSN 1070-9878

Thome, T.; Braga, D. & Blaise, G. (2004). Effect of current density on electron beam induced charging in sapphire and yttria-stabilized zirconia. *Journal of Applied Physics*, Vol. 95, No. 5, (March 2004), pp. 2619-2624, ISSN 0021-8979

Tiku, S. K. & Kröger, F. A. (1980). Effects of space charge, grain-boundary segregation, and mobility differences between grain boundary and bulk on the conductivity of polycrystalline $Al_2O_3$. *Journal of the American Ceramic Society*, Vol. 63, No. 3-4, (March 1980), pp. 183-189, ISSN 1551-2916

Touzin, M.; Goeuriot, D.; Guerret-Piécourt, C.; Juvé, D. & Fitting, H. -J. (2010). Alumina based ceramics for high-voltage insulation. *Journal of the European Ceramic Society,* Vol. 30, No. 4, (March 2010), pp. 805-817, ISSN 0955-2219

Vallayer, B.; Blaise, G. & Treheux, D. (1999). Space charge measurement in a dielectric material after irradiation with a 30 kV electron beam: Application to single-crystals oxide trapping properties. *Review of Scientific Instruments*, Vol. 70, No. 7, (July 1999), pp. 3102-3112, ISSN 0034-6748

Zarbout, K.; Moya, G. & Kallel, A. (2005). Determination of the electron beam irradiated area by using a new procedure deriving from the electron beam lithography technique. *Nuclear Instruments and Methods in Physics Research Section B: Beam Interactions with Materials and Atoms*, Vol. 234, No. 3, (June 2005), pp. 261-268, ISSN 0168-583X

Zarbout, K.; Si Ahmed, A.; Moya, G.; Bernardini, J.; Goeuriot, D. & Kallel, A. (2008). Stability of trapped charges in sapphires and alumina ceramics: Evaluation by secondary electron emission. *Journal of Applied Physics*, Vol. 103, No. 5, (March 2008), pp. 054107(1-7), ISSN 0021-8979

Zarbout, K.; Moya, G.; Si Ahmed, A.; Damamme, G. & Kallel, A. (2010). Study of discharge after electron irradiation in sapphires and polycrystalline alumina. *Journal of Applied Physics*, Vol. 108, No. 9, (November 2010), pp. 094109(1-8), ISSN 0021-8979
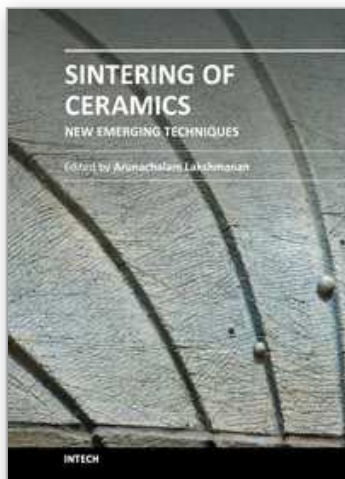
**Sintering of Ceramics - New Emerging Techniques**

Edited by Dr. Arunachalam Lakshmanan

The chapters covered in this book include emerging new techniques on sintering. Major experts in this field contributed to this book and presented their research. Topics covered in this publication include Spark plasma sintering, Magnetic Pulsed compaction, Low Temperature Co-fired Ceramic technology for the preparation of 3-dimesinal circuits, Microwave sintering of thermistor ceramics, Synthesis of Bio-compatible ceramics, Sintering of Rare Earth Doped Bismuth Titanate Ceramics prepared by Soft Combustion, nanostructured ceramics, alternative solid-state reaction routes yielding densified bulk ceramics and nanopowders, Sintering of intermetallic superconductors such as MgB2, impurity doping in luminescence phosphors synthesized using soft techniques, etc. Other advanced sintering techniques such as radiation thermal sintering for the manufacture of thin film solid oxide fuel cells are also described.

**How to reference**

In order to correctly reference this scholarly work, feel free to copy and paste the following:

Zarbout Kamel, Moya Gérard, Si Ahmed Abderrahmane, Damamme Gilles and Kallel Ali (2012). Effects of the Microstructure Induced by Sintering on the Dielectric Properties of Alumina, Sintering of Ceramics - New Emerging Techniques, Dr. Arunachalam Lakshmanan (Ed.), ISBN: 978-953-51-0017-1, InTech, Available from: http://www.intechopen.com/books/sintering-of-ceramics-new-emerging-techniques/effects-of-the-microstructutre-induced-by-sintering-on-the-dielectric-properties-of-alumina

# INTECH

open science | open minds